steel research international
www.steel-research.de

Damage Evolution and Microstructural Fracture Mechanisms Related to Volume Fraction and Martensite Distribution on Dual-Phase Steels

Diego Fernando Avendaño-Rodríguez, Rodolfo Rodriguez-Baracaldo, Sebastian Weber, and Lais Mujica-Roncery*

The scope of this work is the analysis of the damage evolution and microstructural fracture mechanisms of dual-phase steels through quasi-static uniaxial and cyclic tensile tests, considering the influence of the volume fraction and distribution of martensite. The samples are intercritically annealed at different temperatures to obtain three different martensite volume fractions (MVF). Damage evolution is evaluated as a function of stiffness loss. The steels show lower ductility and strength under cyclic loading conditions. The work hardening rate is affected by MVF in different stages of the deformation. A higher MVF is linked to a prompter damage evolution rate. The primary void nucleation mechanisms are ferrite-martensite and ferrite–ferrite decohesion. Martensite fracture can be activated depending on MVF and martensite distribution along the ferrite grain boundary. The dislocation density on grain boundaries is high due to the austenite–martensite transformation during the quenching process and subsequent plastic deformations. Dislocation density is related to stored strain energy, stress concentration, and the observed fracture mechanisms, particularly near martensite grains. Nanoindentation is conducted to evaluate the ferrite and martensite hardness, which depends on its carbon content. It is observed that the martensite/ferrite hardness ratio affects the uniform elongation of the material.

1. Introduction

Currently, the steel manufacturing industry faces significant challenges in meeting the necessary processing requirements to develop low-weight and high-strength materials through efficient and clean production routes. For example, in the transportation and automotive manufacturing industries, lightweight structural materials that enhance the autonomy versus fuel consumption ratio, improve passenger safety, and optimize processing costs, are increasingly a mandatory requirement in the research and development of recent manufacturing projects.[1] In this sense, the development of advanced high-strength steels (AHSS), particularly dual-phase steels (DP), has enabled the improvement of automotive engineering safety through the use of sheet metal members (safety cage components, roof rails, and rear shock reinforcements) with thin walls to improve crashworthiness.[2,3]

Low-carbon dual-phase steels consist of a ferrite matrix and a second phase of distributed martensite. The two phases combined, usually produced by intercritical heat treatments (IHT) and water quenching, are responsible for the plastic flow mechanism observed in these steels.[4,5] Shear stresses are generated along grain boundaries due to the austenite to martensite transformation during the quenching process. Therefore, due to these microstructure volume changes, dislocation density increases.[6,7] As a result, a pile-up of sliding unanchored dislocations reduces yield stress and interacts to produce a high work-hardening rate.[8] Hence, the continuous plastic flow behavior evidenced by dual-phase steel results from the above-mentioned factors.[9] The deformation process of

D. F. Avendaño-Rodríguez, R. Rodriguez-Baracaldo
Grupo de Innovación en Procesos de Manufactura e Ingeniería de Materiales (IPMIM)
Universidad Nacional de Colombia – Bogotá
Car 30 No 45-03, Bogotá D.C., Colombia
E-mail: rodriguezba@unal.edu.co

D. F. Avendaño-Rodríguez
Grupo de Diseño Avanzado
Fundación Universidad de América
Avda Circunvalar No. 20-53, Bogotá D.C., Colombia

The ORCID identification number(s) for the author(s) of this article can be found under https://doi.org/10.1002/srin.202200460.

DOI: 10.1002/srin.202200460

S. Weber
Institut für Werkstoffe
Ruhr-Universität Bochum
Lehrstuhl Werkstofftechnik, D-44780 Bochum, Germany

L. Mujica-Roncery
Grupo de Investigación en Materiales Siderúrgicos e INCITEMA
Universidad Pedagógica y Tecnológica de Colombia
Avenida Central del Norte 39-115, Tunja, Boyacá, Colombia

dual-phase steels can be subdivided into four stages: 1) both phases undergo elastic straining, 2) ferrite is plastically deformed (depending on martensite distribution and volume fraction), 3) both phases are plastically deformed, and finally, 4) fracture of martensite or decohesion along ferrite–martensite interface grain boundary takes place.[6,10] The dual-phase microstructure confers a mechanical behavior characterized by deformation constraint, low yield ratio, continuous-yielding, work-hardening, high tensile strength, high fatigue resistance, pronounced bake hardening, weldability, good ductility, and formability.[11,12]

Some factors influencing dual-phase steel ductile behavior are chemical composition (primarily carbon, manganese, chromium, and silicon content),[13–17] grain size,[18] load direction relative to grain orientation,[19] morphology, and phase distribution.[20] It is well established that the martensite volume fraction (MVF) plays a crucial role in dual-phase steels plastic deformation, and it has been observed that the best results are obtained with small martensite grain size, uniformly distributed in the ferrite matrix (20–40% martensite volume fraction).[21,22] Pakzaman et al. stated that microstructure volume fraction, phase distribution, and morphology limit the deformation process and the stress partitioning.[23] Furthermore, the authors of the current study have previously documented that increasing the amount of martensite in the ferrite matrix increases the dual-phase steel mechanical response under dynamic impact conditions[24] and fatigue.[25]

Due to the intercritical heat treatment temperature range used in the dual-phase steel production, the diffusion mechanism is less effective in transporting interstitial carbon atoms, so the resulting martensite produced during the quenching process has lower yield stress and hardness because of the lower and heterogeneous distribution of carbon content.[26] Moreover, recent research indicates that adding some alloying elements such as vanadium, increases martensite softening. Vanadium addition promotes the formation of carbides inside the martensite phase, which enhances ductility while decreasing hardness due to a reduction in available carbon in the solid solution. Vanadium also allows grain refining, improving ductility and fracture toughness while limiting damage mechanisms to small voids along grain boundaries.[27] Recent studies also indicate that the martensite morphology significantly impacts its resistance to void nucleation, particularly when it has a platelet morphology and the elongated grain is oriented toward the loading direction.[28] According to Ismail et al., martensite platelet-like grains improve strain hardening capacity, but this effect depends on the martensite phase distribution.[29]

The increased damage to the microstructure limits ductility during the plastic deformation process caused by void concentration, coalescence, and subsequent crack propagation.[30–32] It has been reported that damage nucleation occurs primarily at the ferrite–martensite interface and to a lower extent by martensite fracture. It is outlined that a uniform martensite distribution reduces the void growth rate.[20,33,34] However, more recent studies show that the load direction and banded martensite microstructure are critical factors in the fracture mechanism when the steel exhibits this microstructural characteristic.[35] Some researchers report that grain boundary sliding and crystallographic slip contribute to the overall microstructure deformation, emphasizing that grain boundary sliding is an essential mechanism for lath martensite deformation.[36] Moreover, where martensite and ferrite start a simultaneous plastic deformation, void nucleation is arrested, improving the dual-phase mechanical strength.[37] Due to the number of complex factors that influence the damage process of dual-phase steels, some authors have concluded that the statement of a general rule of failure mechanisms is not applicable, and the study should particularize the relationship between the most relevant damage parameters associated with a specific failure mechanism.[38]

Different techniques have been implemented to measure the ductile damage evolution inside a material. Some techniques focus on detecting and measuring voids in a fractured specimen cross-section and estimating its area or volume fraction.[39,40] In addition, the damage can also be measured by the variation in density before and after the material deformation. The voids and cracks reduce the effective material cross-sectional area. Therefore, the increase in the defect volume reduces the final material density, and the measurement of these variations can represent the accumulated damage.[41] An alternative method is measuring the material elastic modulus change at various stages of damage evolution using sound velocity propagation.[42] A material modulus of elasticity is proportional to its density and to the square of the speed of a sound wave transmitted through it. Therefore, measuring the sound velocity transmission in the material cross-section makes it possible to evaluate elastic modulus change after a deformation process and accumulated material damage. The methods outlined before are simple to implement, but the accumulated damage measure variability is significant and may be subject to approximations and several error sources.[43] X-ray computed tomography (XCT) has recently been used for quantitative damage analysis. XCT allows the detailed estimation of microvoids and dimples density, their volume fraction, and distribution on a fracture surface. Some researchers have used this technique to quantify void nucleation,[44] coalescence,[45] and the effect of void size on stress–strain distribution, damage, and fracture in dual-phase steels.[27,46]

Nanoindentation has been used as an alternative method to evaluate the accumulated damage after applying a succession of plastic deformation steps. Using this technique to evaluate the elasticity modulus of the indented microstructure is possible. However, before the indentation measurement, the microstructure deformation effect can generate systematic errors in hardness values due to some factors: strain hardening, grain shape change, texture development, residual stresses, and indentation pile-up effect. These factors artificially increase the local hardening measurement mainly by a high density of grain boundaries underneath the indenter tip, crystal orientation, and dislocation pile-up at grain boundaries.[47–49] Another mechanical method to estimate the cumulative ductile damage evolution is measuring the progressive stiffness loss at an inelastic strain level. A uniaxial cyclic tensile test is needed to obtain a relationship between the isotropic damage on a ductile material versus plastic strain.[50–53] The damage evolution can be estimated using Equation (1), where E^* is the modulus of elasticity of an individual unloading cycle, and E is the dual-phase steel modulus of elasticity. Therefore, the cumulative damage evolution can be plotted against the true strain per cycle, and the resultant curve

represents the progressive decrease of stiffness due to each deformation cycle.

$$\Omega = 1 - \frac{E^*}{E} \quad (1)$$

The uniaxial cyclic tensile test was explicitly used in prior studies to evaluate ductile damage and enhance models used in the spring-back calculation. However, there are different reported methodologies to evaluate the effect of plastic deformation on damage evolution and the elastic modulus reduction from the uniaxial cyclic tensile. Some authors use the chord modulus measurement, i.e., the slope between the minimum and maximum cyclic loop points.[54] Govic et al. added to the chord modulus analysis the instantaneous tangent modulus evaluation to characterize the nonlinearity of the unloading loop.[55] Zhu et al. implemented quasi-plastic-elastic strain models to represent the unloading loop curve accurately.[56] Another approach is to discard the nonlinear portions of the loop and determine the unloading slope by a linear regression method.[43] An additional aspect provided by Kim et al. is that baking heat treatment and strain rate has no significant effect on the unloading response of dual-phase steels.[57]

Despite the scientific work in this field, previous research focuses either on computational models of ductile damage behavior or on plastic deformation in manufacturing processes. The correlation between heat treatment, microstructure, plastic deformation, damage evolution, and its mechanisms is yet to be analyzed holistically. In the current work, cyclical uniaxial tensile tests are employed to directly measure ductile damage in dual-phase steels. The accumulated damage during the deformation process is determined by proposing a simplified method of calculating the modulus of elasticity in each single unloading cycle. In addition, the correlation between cyclic uniaxial deformation and the process of plastic deformation in the microstructure is presented in detail. The same dual-phase steel composition with different martensite volume fractions was examined. A correlation was established between fracture mechanisms, morphology, grain orientation concerning the load direction, and martensite carbon content. In this study, the following experimental techniques were used: damage measurement by elastic modulus degradation, nanoindentation, scanning electron microscopy, and electron backscattering diffraction.

2. Experimental Section

2.1. Material

A 3.4 mm industrially produced hot rolled dual-phase sheet was studied. The chemical composition is given in **Table 1**. The chemical analysis was determined using optical emission spectroscopy (OES).

Table 1. Chemical composition of dual-phase steel in wt%. Fe balance.

C	N	Mn	Cr	Si	P	S
0.066	0.0022	1.219	0.135	0.988	0.011	0.007

2.2. Heat Treatment

Thermodynamic calculations were performed using the TCFE9 (steels/Fe alloys) database of Thermo-Calc (Thermo-Calc Software AB, Solna, Sweden). This analysis made it possible to conclude that the intercritical annealing temperatures are found between 703 and 883 °C for the alloy composition in Table 1. In addition, the carbon content of the phases was determined under equilibrium conditions.

All specimens were cut in the rolling direction (RD) using the laser cutting process. Geometries agree with ASTM E8[58] and ASTM E466[59] standards, respectively. Two of the abovementioned sample groups were reserved for mechanical testing on the as-received material (AR1), while the other four were heat treated.

Sample groups were then subjected to two different processing schedules to develop a dual-phase microstructure with different martensite volume fractions. First, the steel was heated to 975 °C in a tubular furnace Thermolyne 21 100 for 35 min, using a heating rate of 0.6 °C s^{-1}, followed by brine quenching to room temperature (10% NaCl in aqueous solution). With this procedure, the resulting microstructure is fully martensitic. Second, a sample group was subjected to intercritical temperatures of 812.5 °C (heat treatment two, HT2) and another sample group, at 839.3 °C (heat treatment three, HT3) in the tubular furnace for 30 min followed by brine quenching to room temperature. The tubular furnace was adapted to permit the vertical drop of specimens to the brine bath. The falling time for the total immersion of each specimen was approximately 0.4 s. Decarburization was prevented by applying an industrial protective coating ATP-641 with a service temperature range between 800 and 1,250 °C.[60] All the specimens were coated twice before the heat treatments.

2.3. Microstructure Characterization

After heat treatment, all samples were prepared by standard mechanical grinding with SiC paper and polishing procedures, finishing with 1.0 μm diamond suspension. After polishing, the specimens were etched for 10 s in a 3% Nital solution. The microstructures of the etched specimens were observed employing optical microscopy (OM) on an Olympus BX60M and scanning electron microscopy (SEM) with a TESCAN MIRA3. Using a MATLAB algorithm developed by Murillo-Barraza et al.,[61] grain size and volume fraction measurements were conducted to analyze three micrographs by each specimen.

When using optical microscopy, the material presents a dual-phase microstructure consisting of a light ferrite matrix and dark martensite dispersed grains. The as-received material micrograph taken from the transverse direction is shown in **Figure 1**a,d.

Ferrite grain size (FGS) was determined following the ASTM E112 standard guidelines. Martensite volume fraction (MVF), martensite grain size (MGS), and martensite mean free path (MMFP) were determined following the ASTM E112,[62] and ASTM E1245[63] standards guidelines and, through the implementation of a MATLAB algorithm developed to conduct the automatic measurement of phase properties by digital image

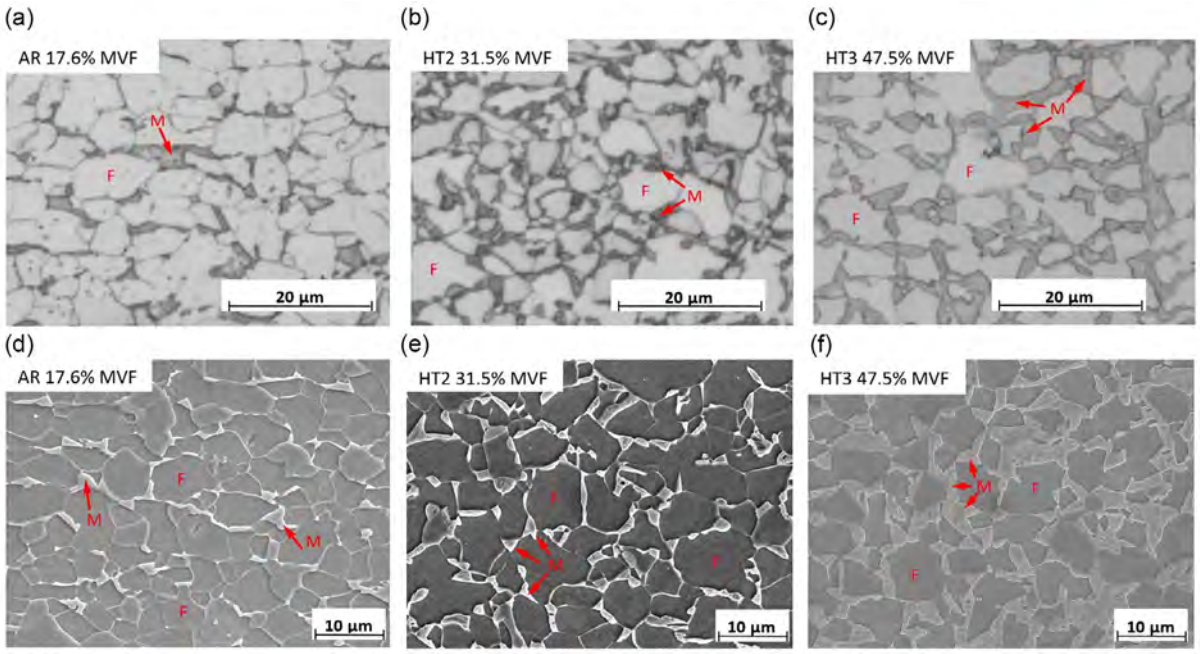

Figure 1. Material micrographs, taken in a transverse plane perpendicular to the rolling direction. Optical micrographs: a) As-received material (AR1) 17.6% MVF, b) heat treatment two (HT2) 31.5% MVF, c) heat treatment three (HT3) 47.5% MVF. SEM micrographs: d) AR1 17.6% MVF, e) HT2 31.5% MVF, (f) HT3 47.5% MVF. F denotes ferrite and M denotes martensite.

processing.[64] The values reported correspond to the averages obtained in analyzing three micrographs per specimen. A process example used to perform the microstructural analysis can be seen in **Figure 2**. The material micrograph image is first segmented using a MATLAB algorithm, separating ferrite, martensite, and grain boundaries. Then, the three segmentations are subsequently combined, and the software estimates the grain sizes of each phase based on the occupied area in the image.

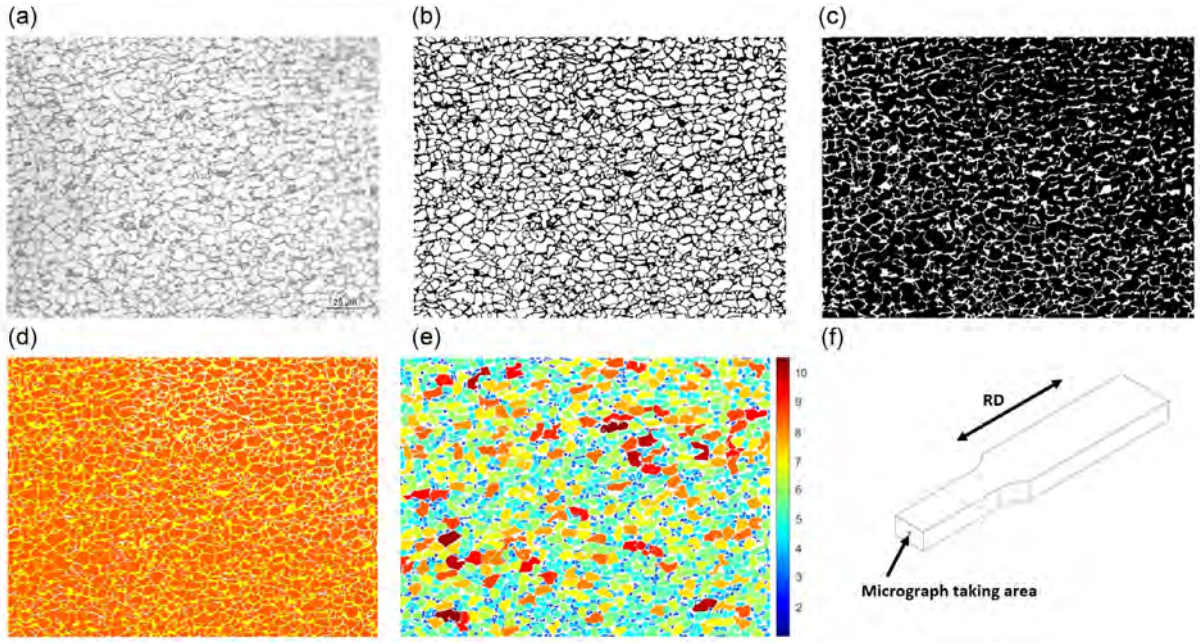

Figure 2. AR1 material microstructural MATLAB analysis. The specimen is taken in a transverse plane perpendicular to the rolling direction. Ferrite, martensite, and grain boundary segmentation were considered independently. a) Complete dual-phase steel optical micrograph, b) ferrite segmentation (white), c) martensite segmentation (white), d) phase segmentation union (orange—ferrite, yellow—martensite, grain boundaries—white), e) ferrite grain size measurement µm, (f) micrograph taking area. RD, rolling direction.

2.4. Hardness Measurements

The primary constituent hardness (ferrite and martensite) was evaluated from the load-penetration depth curves obtained in a nanoindentation tester Nanomechanics Inc. iMicro, with a Berkovich diamond indenter. The indentations were made to a maximum load of about 20.0 mN and an indentation depth of 450 nm.

For each material specimen, one hundred grid indentations were made on one specimen. Subsequently, the specimens were etched with a 3% Nital solution for 10 s. **Figure 3** shows an optical micrograph of the 10 × 10 nanoindentation test pattern on an HT3 specimen with a step size of 10 μm. The specimen is taken from the rolling direction plane, and white arrows indicate the nanoindentation sequence. Each indentation was identified and classified using optical microscopy to define the hardness within the respective phases. In addition, nanoindentation depth and deformation energy were also considered as classification factors to determine the hardness level of each phase.

2.5. Mechanical Tests

Two experiments were conducted to evaluate the dual-phase mechanical behavior: quasi-static uniaxial tensile and uniaxial cyclic tensile test. Tensile specimens were prepared according to the ASTM E8 standard with a gauge length of 25 mm (**Figure 4**a), and uniaxial cyclic test specimens are in agreement with the ASTM E466 standard (Figure 4b). The uniaxial cyclic tensile test was programmed to perform 33 cycles, and four were defined with a minor deformation step near the elastic zone. In all the specimens, the total fracture was achieved after this process. Mechanical testing was performed at a constant crosshead displacement rate of 1.0 mm min^{-1} using a Shimadzu UH-500kNI hydraulically driven machine. The strain measurement was made with an Epsilon 3542 axial extensometer of 25 mm gauge length. The strain hardening exponent (n) was determined

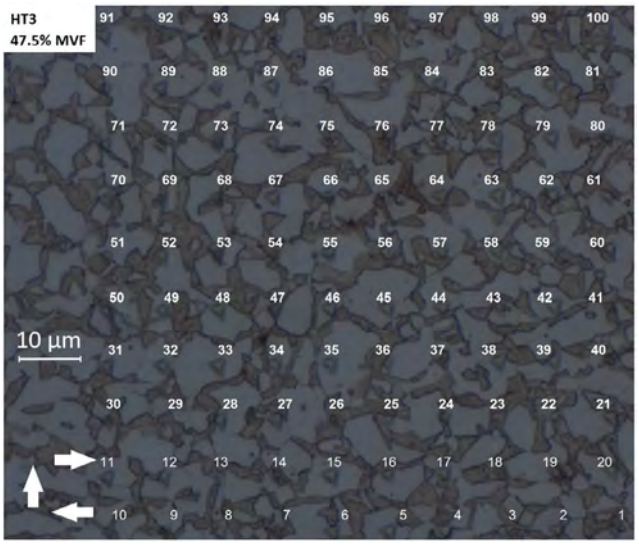

Figure 3. Optical micrograph of the 10 × 10 nanoindentation test pattern on a HT3 specimen.

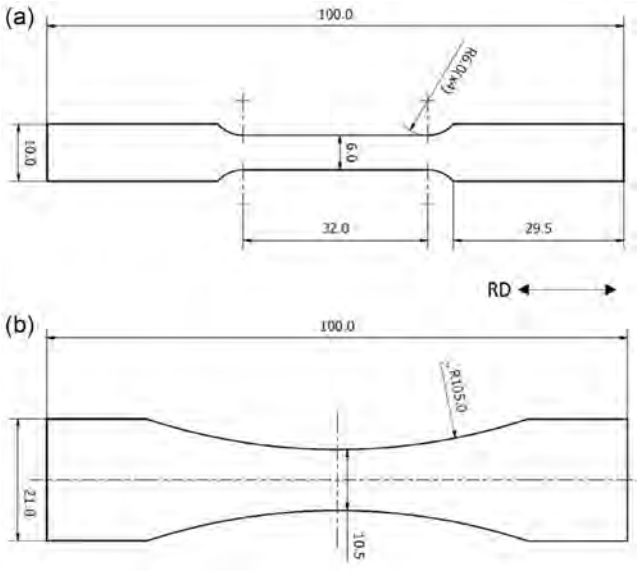

Figure 4. Test specimen geometries. a) Quasi-static uniaxial tensile test ASTM E8, b) Uniaxial cyclic tensile test ASTM E466. RD, rolling direction.

using the guidelines of the ASTM E646 standard,[65] using the strain data from 0.2% to the uniform strain of each material.

2.6. Microstructure Plastic Behavior

A specimen for each type of material was prepared metallographically along the loading direction to study the microstructural plastic deformation after the quasi-static uniaxial tensile and cyclic tensile tests. The surface was explored from the fracture zone to an undeformed zone using OM and SEM. The fracture surface was studied by SEM and stereoscopic analysis on a KEYENCE VHX-600.

The SEM TESCAN MIRA3 was equipped with an Oxford Instruments electron backscattered diffraction (EBDS) detector combined with AZtec 3.1 analysis software. The EBSD parameters were an accelerating voltage of 20 kV with a beam current of 1.7 nA and a step size of 85 nm, which resulted in high indexing success. Therefore, no image processing was necessary to clean the resulting EBSD data. Instead, different EBDS maps, including Image quality (IQ), inverse pole figure (IP), and Kernel average misorientation (KAM), were implemented to characterize the deformed sections near the fracture zone.

The specimens were prepared in the following way to apply the EBSD technique: first, they were ground with SiC up to 2000 grit sandpaper and polished with 3.0 μm diamond suspension at 2.0 bar to 150 rpm contra rotation for 15 min and lubricated with blue lube ethanol (BLUE) based lubricant. Second, the specimens were polished with a 1.0 μm diamond suspension at 2.0 bar to 150 rpm contra rotation for 10 min and lubricated with BLUE. Third, they were polished with a 0.25 μm oxide polishing suspension (OPS) at 2.0 bar to 100 rpm contra rotation for 5 min and lubricated with distilled water. The final stage was vibratory polishing on a VibroMet 2 using a 55% aqueous solution of 0.02 μm noncrystallizing colloidal silica polishing suspension

(MasterMet 2), with a counterclockwise, 20% amplitude by 7 h. The surface cleaning was done by ethyl alcohol jet and cotton.

3. Results and Discussion

3.1. Thermal Treatment

The Thermo-Calc equilibrium conditions analysis results are shown in **Figure 5**. Based on the experimental martensite volume fractions, the heat treatment temperatures can be verified from the austenite curve in the phase equilibrium diagram that is shown in Figure 5a. These results are in good agreement with experimental parameters (see **Table 2**). Furthermore, from Figure 5b, the austenite (martensite) carbon content can be estimated. An inverse relationship between carbon concentration and martensite volume fraction can be observed, implying that the martensite reduces its hardness by increasing the intercritical heat treatment temperature. Mazaheri et al. reported a similar trend producing a dual-phase microstructure from an AISI 5115 steel.[66] The intercritical temperature was 770 °C (similar to our AR1 condition), but the holding time was increased from 8 to 14 min in 2 min intervals. The holding time change results in a martensite volume fraction increase but causes a reduction in martensite carbon content and hardness.[66] Because the diffusion process is a time and temperature-dependent phenomenon, martensite carbon content is reduced with these two factors. Hence, martensite decreases in hardness with increasing volume fraction. Table 2 summarizes the carbon content of the phases evaluated at equilibrium conditions. The results indicate that increasing the intercritical temperature increases the martensite volume fraction at a constant steel chemical composition and intercritical holding time. In Table 2, the temperatures and phase carbon content were estimated using a Thermo-Calc equilibrium conditions analysis, whereas the martensite volume fraction and microstructural parameters were obtained experimentally.

Table 2. Material microstructural properties.

State	IHT[a)]	MVF[b)]	MGS[c)]	MMFP[d)]	FGS[e)]	α CC[f)]	γ CC[g)]
	[°C]	[%]	[μm]	[μm]	[μm]	[wt%]	[wt%]
AR1	768.9	17.6	1.5	35.7	3.4	0.0091	0.3285
HT2	812.5	31.5	2.3	8.4	3.3	0.0069	0.1926
HT3	839.3	47.5	2.5	2.8	3.3	0.0056	0.1321

[a)]Intercritical heat treatment (IHT); [b)]Martensite volume fraction (MVF); [c)]Martensite grain size (MGS); [d)]Martensite mean free path (MMFP); [e)]Ferrite grain size (FGS); [f)]Ferrite carbon content (α CC); [g)]Austenite carbon content (γ CC).

3.2. Microstructural Characterization

The as-received and heat-treated materials present a ferrite matrix with lath martensite grains distributed at the grain boundaries. On the as-received material, the ferrite grain sizes are in the range of 2.0–5.0 μm with a uniform distribution of this phase and dispersed martensite grains with a 17.6% MVF (Figure 1a,d). As mentioned by other authors, this phase distribution anticipates a very ductile behavior in terms of uniform plastic deformation in this material.[37] In particular, the martensite mean free path indicates that this phase is dispersed in the microstructure, reducing material strain hardening (see Table 2).

HT2 steel presents a remarkably similar distribution of ferrite grain sizes. However, an increase in the size and amount of interconnected martensite grains is distinguished at the grain boundaries (Figure 1b,e). In addition, an increase in MVF up to 31.5% can be observed while the martensite grain size increases and its mean free path is reduced. This new microstructural configuration favors strain hardening while ductility is reduced. Finally, HT3 steel presents a homogeneous distribution of ferrite and martensite grains, where martensite reduces the ferrite–ferrite interface with a 47.5% MVF (Figure 1c,f).

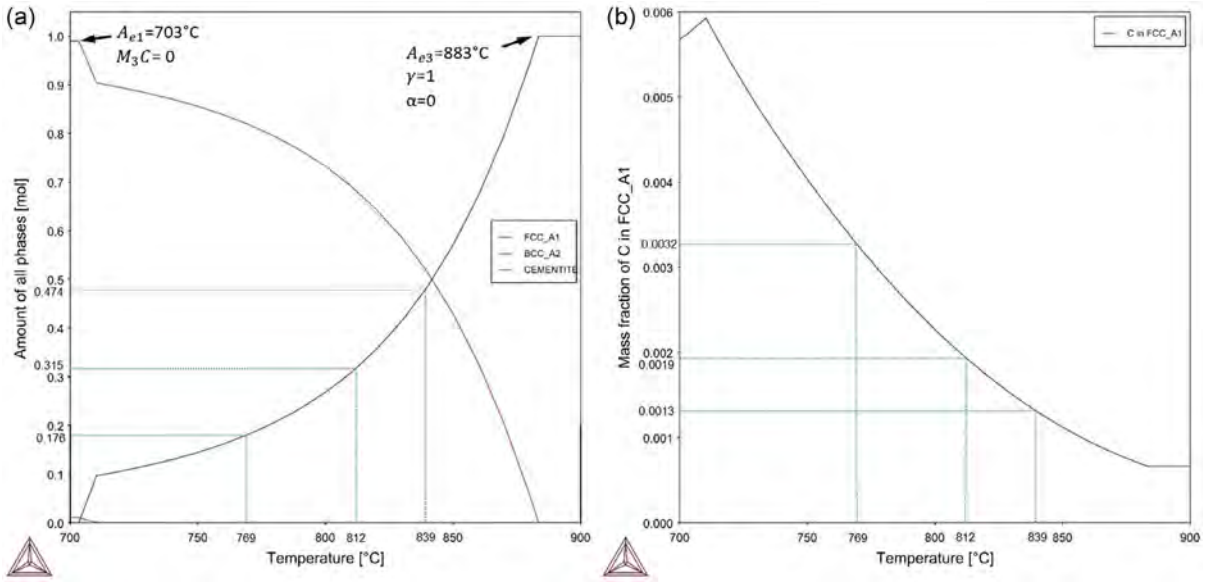

Figure 5. Thermo-Calc equilibrium conditions analysis. a) Phase equilibrium diagram, b) austenite carbon content diagram.

The martensite mean free path is equivalent in dimension to grain size, indicating that the martensite grains are close together, favoring ductility reduction and an initial high-strain hardening behavior. Gorain et al. started from hypereutectoid steel with similar chemical composition and obtained equivalent microstructures and mechanical behavior with an analogous heat-treatment process.[67]

3.3. Quasi-Static Uniaxial Tensile Test

The tensile test results are reported in **Table 3**, the presented values are the average of five specimens, and the experimental flow curves for dual-phase steels are shown in **Figure 6**a. The curves show that the ultimate tensile strength (UTS) increases with increasing martensite volume fraction, reducing the ductility. The typical dual-phase continuous yielding behavior and low yield stress/ultimate tensile strength ratio are also observed for the as-received and heat-treated materials.

It has been reported that this behavior results from mobile geometrically necessary dislocation (GND) produced at the ferrite–martensite interface, which glides into ferrite grain boundaries. This process is initially induced by the volume expansion during austenite–martensite transformation and is activated later during plastic deformation.[67] Due to the deformation process, ferrite grains are elongated in the loading direction, reducing the dislocation glide path and increasing cross-slip, and pile-up over grain boundaries, resulting in an enhanced material strain hardening behavior.[67] Recent contributions indicate that most martensite dislocations in Fe–C steels are heavily segregated with carbon and may not be mobile during the deformation process. Therefore, a newer explanation of continuous martensite yielding suggests considering this phase as a multiconstituent composite,[68] where strain hardening is caused by constituents yielding and not by dislocation multiplying. Combining the two proposed mechanisms can explain the hardening process observed in dual-phase steels. Furthermore, additional studies, like the one by Zhang et al.,[69] have investigated the influence of carbon content on martensite and discovered that at low carbon concentrations (0.17 wt%), it tends to segregate at grain boundaries and in geometrically necessary dislocations. In addition, the distribution of carbon between grain boundaries, dislocations, and interstitial spaces is more uniform when it ranges between 0.17 and 0.35 wt%, promoting the formation of more ordered martensite.[69] The initial strain-hardening effect of the material increases with martensite volume fraction, and this can also be observed in Table 3 with the parameters of strength

Table 3. Quasi-static uniaxial tensile test results.

State	–	$\epsilon y^{a)}$	$\sigma y^{b)}$	$\epsilon u^{c)}$	σuts$^{d)}$	RA$^{e)}$	$\sigma f^{f)}$	$\sigma y/\sigma u^{g)}$	$E^{h)}$	UE$^{i)}$	UP$^{j)}$	UT$^{k)}$	$K^{l)}$	$n^{m)}$
		(%)	(MPa)	(%)	(MPa)	(%)	(MPa)	–	(GPa)	(MJ m^{-3})	(MJ m^{-3})	(MJ m^{-3})	[MPa]	–
AR1	$\mu^{n)}$	0.47	549.6	18.5	816.1	69.6	835.8	0.67	201.1	1.8	187.8	189.5	1086.2	0.16
	$\sigma^{o)}$	0.01	11.4	0.18	10.4	2.0	24.0	0.02	0.4	0.08	18.3	18.4	8.3	0.0
HT2	μ	0.40	403.2	11.8	826.8	49.0	870.9	0.48	203.9	1.1	170.2	171.3	1314.3	0.20
	σ	0.01	7.4	1.9	35.3	9.7	7.1	0.03	1.7	0.07	7.5	7.6	32.5	0.01
HT3	μ	0.48	465.1	8.2	866.3	57.2	910.6	0.54	205.8	1.4	157.4	158.8	1595	0.22
	σ	0.09	37.6	0.6	54.3	7.3	91.4	0.04	2.9	0.27	7.7	8.0	149.5	0.02

[a)]Yield strain; [b)]Yield stress 0.2%; [c)]True uniform strain; [d)]True ultimate tensile strength; [e)]Reduction of area; [f)]Fracture stress; [g)]Yield stress/ultimate tensile strength; [h)]Elastic modulus; [i)]Resilience; [j)]Plastic deformation energy; [k)]Specific fracture energy; [l)]Strength coefficient; [m)]Strain-hardening exponent; [n)]Average; [o)]Standard deviation.

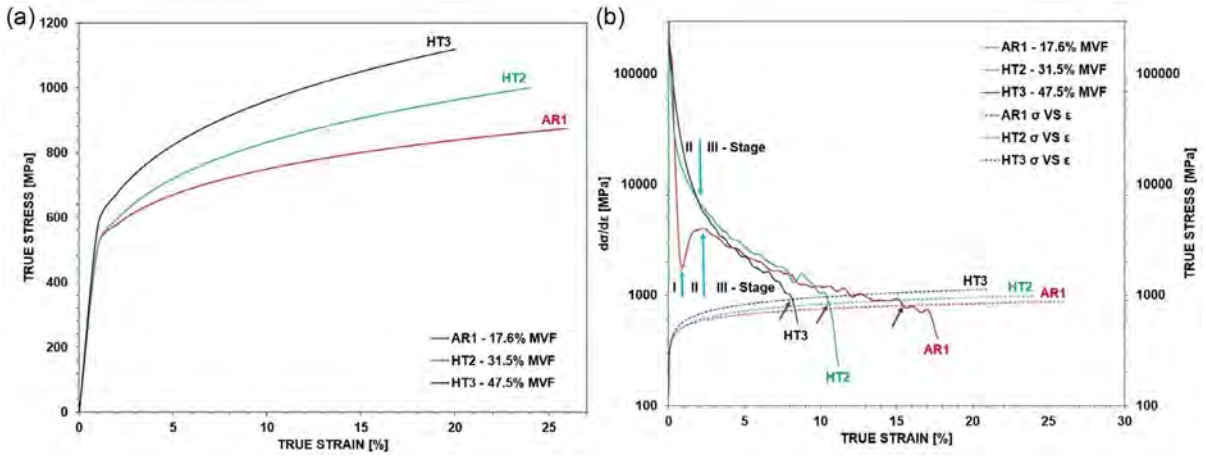

Figure 6. Tensile test: a) true stress–strain curves, b) work-hardening rate versus true strain curves (solid lines) and true stress–strain curves (dotted lines).

coefficient and strain-hardening exponent. Ashrafi et al. reported a similar mechanical behavior regarding the martensite content in the microstructure.[70] Furthermore, Zhang et al. asserted that the strain-hardening ability of dual-phase steels is remarkably affected by martensite fraction and grain morphology, especially at high martensite contents due to toughness and ductility reduction.[22]

The work hardening rate curves for the three materials are shown in Figure 6b combined with the tensile test curves to analyze the Considère criterion. Applying this criterion, the necking point (purple arrows in Figure 6b) agrees with the uniform strain reported in Table 3. The work-hardening behavior of the AR1 material exhibits three stages (I, II, and III), which are delimited in Figure 6b by blue arrows that mark their transition. Ferrite plastic flow and dislocation movement are related to the first stage. According to some authors, the second stage involves the continued ferrite deformation and the potential strain-induced transformation of retained austenite to martensite.[71] Finally, the simultaneous plastic deformation of ferrite and martensite is related to stage three.[71,72] Moreover, HT2 and HT3 materials only show stages two and three (Figure 6b). The HT3 material exhibits the highest work-hardening behavior among the three materials until the third deformation stage starts (black curve in Figure 6b). After this point, the HT2 material exhibits a superior work-hardening behavior (green curve in Figure 6b). Finally, the AR1 steel has the smallest value of n at low strains, as shown in Figure 6b (red curve) and Table 3.

No representative trend was found in the variation of plastic deformation energy between the different materials in the present study. This result may be mainly explained because, although the ultimate tensile strength is increased with the martensite volume fraction, the fracture strain is reduced, resulting in approximately equivalent energy values (Table 3).

3.4. Uniaxial Cyclic Test

Figure 7 shows a typical uniaxial cyclic tensile test, with only the AR1 and HT3 materials shown to better contrast the mechanical behavior. The ultimate tensile strength of the as-received material ultimate tensile strength was near 753 MPa. In contrast, heat treatment material HT2 reached 765 MPa and HT3 830 MPa. Therefore, as can be observed, the ultimate tensile strength in cyclical tests increases as the volume fraction of martensite grows. However, due to this deformation process, a simultaneous ductility and material strength reduction can be observed compared to the typical quasi-static uniaxial tensile test.

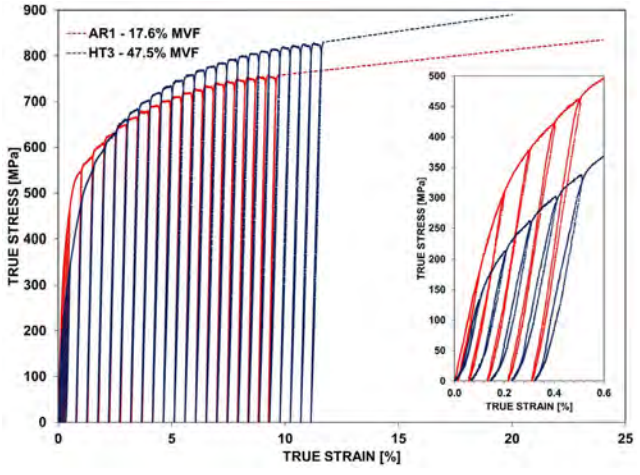

Figure 7. Uniaxial cyclic tensile test curves. The inset of the right side shows the initial cyclic deformation process.

The loading and unloading loops present a nonlinear behavior, and at each deformation step, a higher plastic flow stress is required due to the strain hardening of the steel. Therefore, the area inside the loop represents the energy dissipated due to the deformation process.[56] The nonlinearities of each loop due to plastic deformation were discarded to simplify the unloading module evaluation. Only load range values between 5% and 95% from the unloading leg loop were considered for each deformation step. Subsequently, a linear regression method was used to determine the individual unloading slope of each cycle.[43] The unloading elastic modulus decreases with increasing plastic strain in all three types of materials. Moreover, other researchers have reported similar results, despite differences in carbon concentration and microstructural characteristics.[52] There was a reduction of 10.6% for AR1, 18.8% for HT2, and 13.6% for HT3 when comparing the initial modulus of elasticity of each material with the modulus of elasticity obtained in the unloading cycle at the uniform deformation. Three main factors explain the elasticity modulus degradation: displacement of mobile dislocation and pile-ups near the grain boundaries or solutes, damage evolution due to microcrack generation, and increased residual stresses.[57,73] The shear stress is released during the unloading process, and the dislocation pile-ups are induced into a backward motion. This produces a nonlinear elastic strain recuperation leading to the elastic modulus decrease at each deformation loop. This process is increased with the increment of strain level, grain size, martensite volume fraction, and phase mechanical properties resulting in damage accumulation.[74]

As shown in **Figure 8**a, the cumulative damage can be seen in each material from its original state to uniform deformation. Because necking formation occurs first in all AR1 quasi-static cyclic tensile test specimens, the cumulative damage for this material is only shown until 10% of true strain is reached. Under these deformation conditions, the as-received material presented a lower damage evolution than the heat-treated steels at the same strain level, and this could be explained due to the higher ductility of the former. In addition to more significant damage accumulates on heat-treated samples during the cyclical deformation process due to the higher martensite volume fraction. As is well known, the higher martensite content facilitates the appearance of two typical fracture mechanisms: the ferrite–martensite phase decohesion and the martensite fracture. Consequently, more significant damage due to the progressive loss of stiffness and ductility of the heat-treated steels can be explained by the combination of the higher martensite volume fraction and the fracture mechanisms associated with the martensite. Figure 8b shows a linear relationship between cumulative damage and deformation level after a certain level of true strain has been reached. In contrast to the heat-treated material states, which show this behavior starting at a 2% strain, the as-received material shows this linear behavior more clearly after a 5% strain. This kind of relationship can be included in an

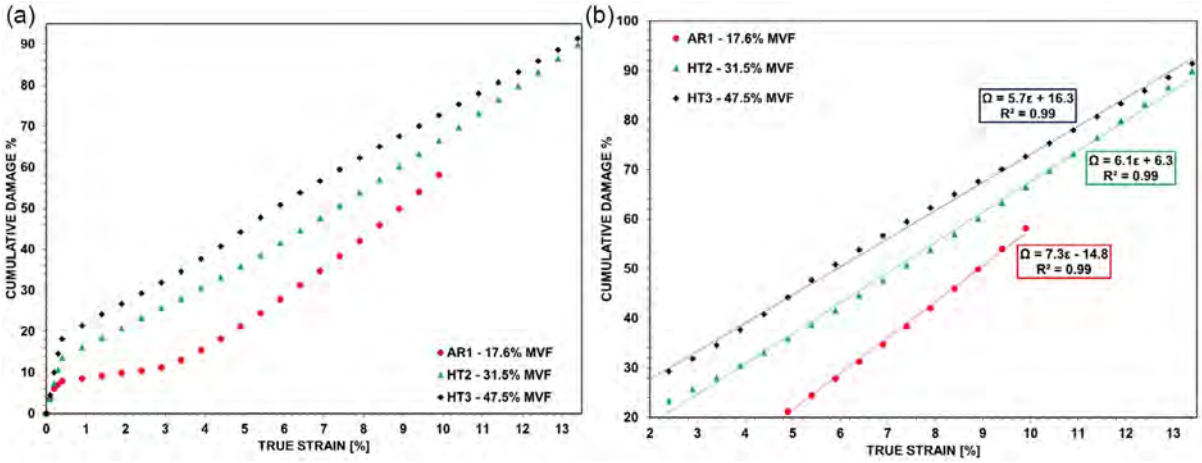

Figure 8. Ductile damage evolution curves: a) measuring the progressive stiffness loss, b) damage linear behavior versus true strain.

elastic-plastic-damage constitutive model to predict the damage progression of the material during a deformation process.

Figure 9 shows the fracture surfaces of specimens from AR1 and HT3 conditions subjected to a quasi-static uniaxial tensile and cyclic tensile test. All images were taken near the center of the specimen. The as-received material has a lower amount of dimples that are uniformly distributed on the fracture surface and with extensive ductile damage (Figure 9a,c). The HT3 material has more dimples, a nonuniform distribution over a more uneven fracture surface, and more minor size dimples at grain boundaries (Figure 9b,d). Depth tear ridges are visible in the HT3 material. The martensite content in the specimens can explain the difference in the surface topography. A more irregular and tortuous fracture is related to a high martensite volume fraction.

When comparing the fracture surfaces concerning the specimen deformation type, an interesting difference appears within the internal surface dimples on the as-received material.

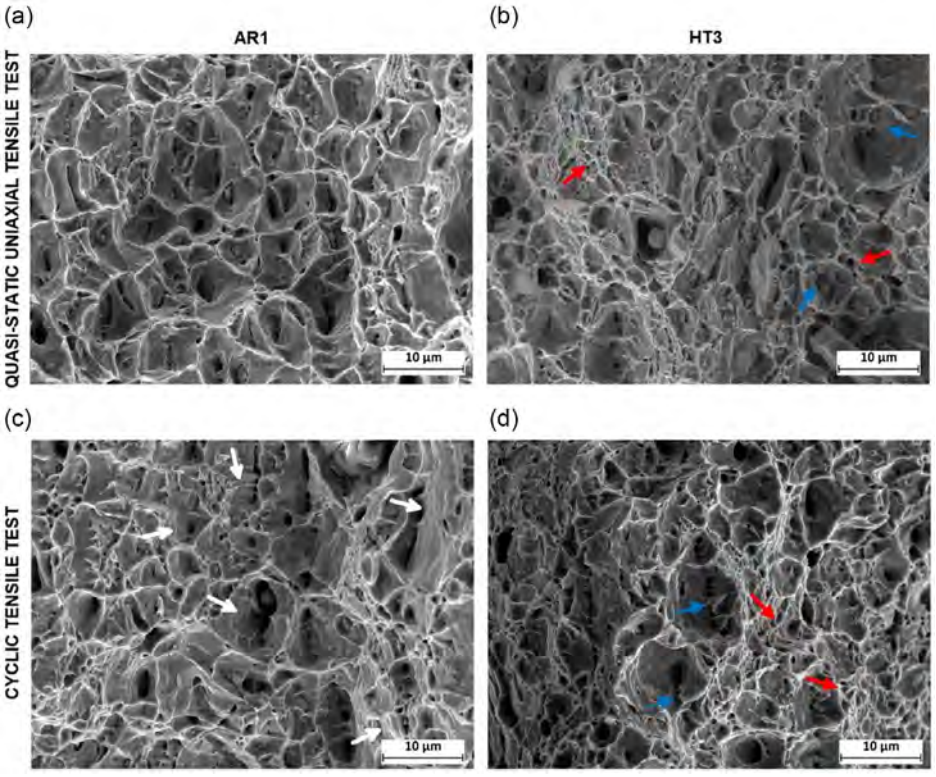

Figure 9. SEM micrographs ductile fracture surface: quasi-static uniaxial tensile test a) AR1 and b) HT3, cyclic tensile test c) as-received and d) HT3. White arrows indicate dimple striations, red arrows indicate low-size dimples, and blue arrows indicate tear ridges.

Qualitatively, wall dimples are smoother on the specimen subjected to the quasi-static uniaxial tensile test (Figure 9a). Meanwhile, in the cyclic specimens, more tortuous deformation and even striations are visible inside the dimple walls (see white arrows in Figure 9c). However, this effect is not visible in the HT3 material due to the higher martensite volume fraction.

3.5. Nanoindentation

Table 4 shows the results of the hardness test. **Figure 10** shows the typical load-penetration depth curves of ferrite and martensite for the three types of materials. The curves show that martensite has a smaller penetration depth and lower deformation energy at constant load. As a result, martensite has a higher hardness in all three materials than ferrite.

The ferrite maintains a uniform grain size as the intercritical temperature rises, although its carbon content and hardness decrease, according to the nanoindentation test (Table 4) and microstructural analysis (Table 2). Furthermore, as the intercritical temperature rises, martensite grain size grows, but carbon content and hardness decrease (Table 4). As shown above, the carbon diffusion process and its content significantly influence microstructural hardness. Mazaheri et al. reported a similar behavior to the present study. Their findings, however, indicate a more pronounced trend toward rising ultimate tensile strength and yield stress with regard to the hardness ratio between martensite and ferrite, which can be attributed to the higher carbon content of the studied steel, and higher martensite carbon content obtained during the heat treatments.[66] It is important to note that when the martensite volume fraction increases, due to the dissolution of carbon in the phases, the hardness of ferrite and martensite decreases (Table 2), as the martensite/ferrite hardness ratio does (Table 4).

It is noteworthy to note that in the case of ferrite, the grain size and hardness obtained remained in a range that was very similar for the three types of dual-phase steels, which is consistent with the low content of soluble carbon in this phase that was estimated by the results of the Thermo-Calc equilibrium conditions analysis. Otherwise, in the case of martensite, the grain size increases while the hardness decreases; this mechanical behavior can be attributed to the reduction of the carbon content in the martensite with little appreciable effect in terms of grain size (Table 2).

The mechanical compatibility of two phases is defined as the hardness ratio. In dual-phase steels, for example, it is the ratio of ferrite and martensite hardnesses. Table 4 shows this factor, denoted by Mc. The mechanical compatibility of the two phases increases as Mc approaches 1.[27] Because Mc is, on average, equal to 0.74, the three materials have similar mechanical compatibility. However, because the martensite grain size increases with the martensite volume fraction, the number of geometrically necessary dislocations also increases. As a result, strain hardening increases. Although martensite gets softer as the heat treatment temperature rises (increasing its ductility), its volume fraction increases, raising the effect of strain hardening on the ferrite grain boundaries and reducing dual-phase ductility. Martensite creates numerous dislocations and subsequently pile-up during the deformation process. According to the prior, a higher martensite volume fraction reduces uniform elongation (**Figure 11**a) while increasing ultimate tensile strength (Figure 11b).

Table 4. Nanoindentation results.

State	MVF[c]	Nanohardness						
		Martensite		Ferrite				
		μ[a]	σ[b]	μ	σ			
		[GPa]				M/F-HR[d]	Mc[e]	M–S[f]
AR1	17.6	5.5	0.3	4.0	0.1	1.39	0.72	
HT2	31.5	5.2	0.2	3.8	0.1	1.37	0.73	6.0%
HT3	47.5	4.6	0.2	3.6	0.1	1.29	0.77	16.0%

[a]Average; [b]Standard deviation; [c]Martensite volume fraction; [d]Martensite/ferrite hardness ratio; [e]Mechanical compatibility; [f]Martensite hardness softening relative to AR1 material.

3.6. Microstructure Evolution Due to Plastic Deformation

Figure 12 shows the optical micrographs on the longitudinal plane along the loading direction on the uniaxial cyclic tensile

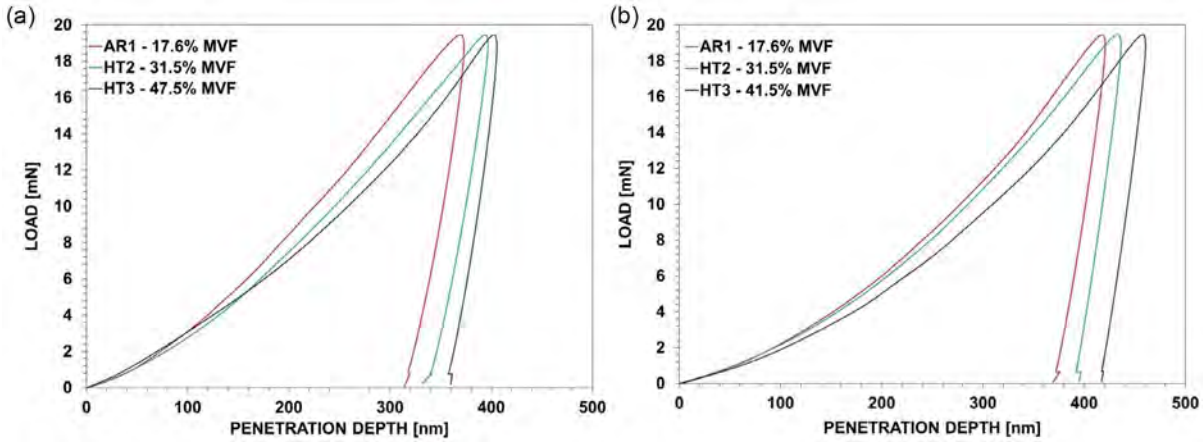

Figure 10. Representative nanoindentation load-penetration depth curves: a) martensite, b) ferrite.

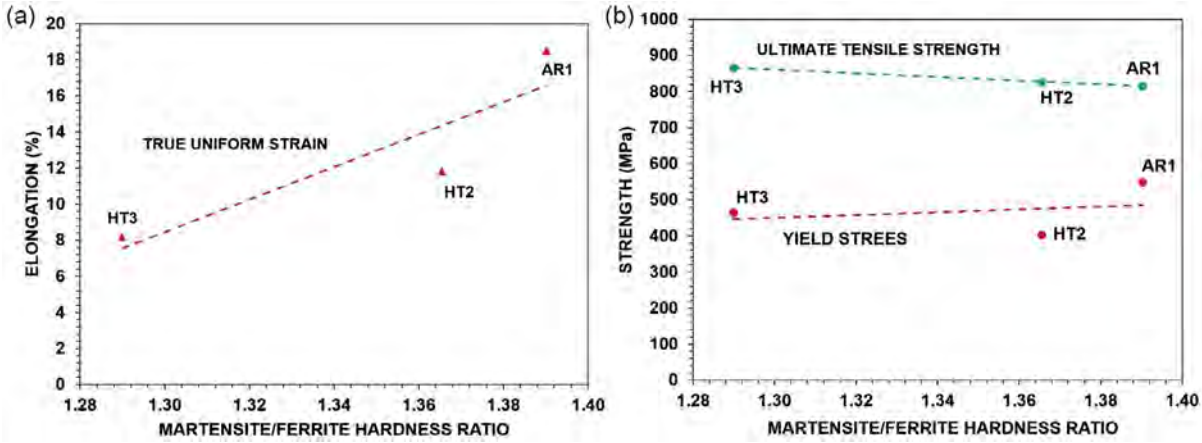

Figure 11. Martensite/ferrite nanohardness ratio, related to mechanical properties: a) elongation vs phases hardness ratio, b) strength vs phases hardness ratio.

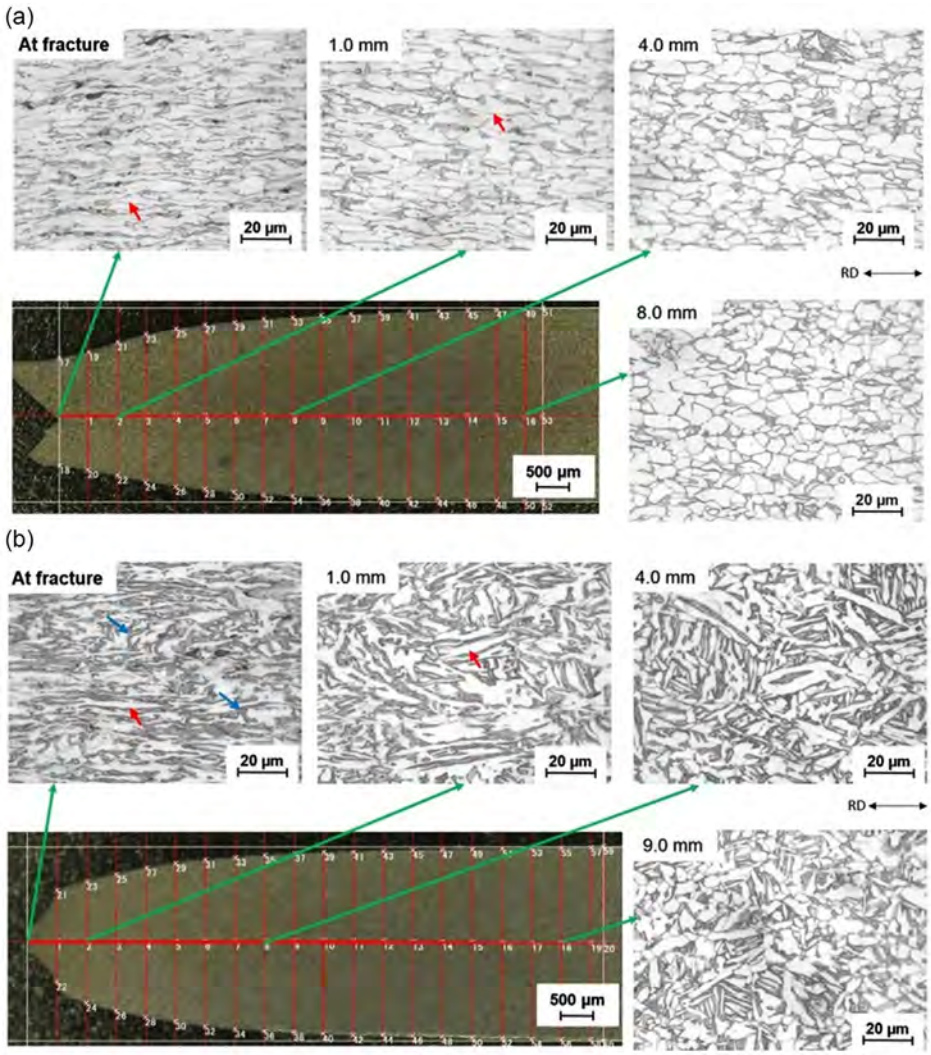

Figure 12. Optical micrographs of plastic deformation on the uniaxial cyclic tensile test specimens. The specimen is taken from the mid-width in the longitudinal plane: a) AR1 17.6% MVF, b) HT3 47.5% MVF. Red arrows—elongated grains, blue arrows—plastic flow obstacles.

test specimens. The boxes at the upper left of each micrograph show the distance from the fracture zone, and the white numbers and red mesh in the images of the fractured specimens show where the thickness of the specimen was measured. The ferrite and martensite grains are substantially elongated around the fracture zone in the as-received material, the thickness reduction is close to 51% (Figure 12a, red arrows), and the damage due to deformation is uniformly distributed on the ferrite matrix. HT3 material presents a similar behavior in the deformation of its microstructure. However, some martensite grains oriented perpendicular to the rolling direction become obstacles to the plastic flow (Figure 12a, blue arrows). This phenomenon has two consequences: a local increase in strain hardening and cumulative damage behind that zone (Figure 12b). It can be seen from these images what is the effect of the microstructure in the plastic deformation process. A material with a low martensite content turns out to be more ductile because the ferrite has greater freedom to flow plastically, while a material with a high martensite content hardens rapidly due to the restriction of plastic flow. It is also interesting that the martensite presents a ductile deformation near the fracture zone. When martensite exhibits a fiber-type or platelet-like shape, as seen in Figure 12b, other researchers have noted similar behavior in dual-phase steels.[29] This phenomenon may be related to the lower hardness and carbon content of martensite, particularly in the HT3 material.

As shown in **Figure 13**, it is possible to observe the fracture mechanisms reported in dual-phase steels: ferrite–martensite and ferrite–ferrite grain boundaries decohesion, martensite fracture, and damage caused by inclusions present in the metal matrix. The first two of these four were the most frequently noticed. Other researchers report the decohesion of the ferrite–martensite interface or the fracture of the martensite grains as the predominant type of fracture.[20,33,34] However, it is essential to consider that some factors such as the chemical composition and the microstructure resulting from the intercritical heat treatment have an essential role in developing fracture mechanisms. Ismail et al. also state that due to the microstructure, the damage process in dual-phase steels is controlled by inhomogeneities in stresses and strains. The main microstructural factors are morphology, orientation, and martensite volume fraction. Emphasis is placed on the propagation of damage by coalescence in two stages, local and large-scale when the martensite has a morphology similar to that of platelets.[29] In steels with higher martensite content and platelet-like morphology, there is higher resistance to the nucleation of microvoids, which can be explained by the influence of ductile deformation of the two phases in the load direction.[28]

Some aspects that should be highlighted concerning the fracture mechanisms and the material type are the following (Figure 13): most voids occur at the ferrite–martensite or ferrite–ferrite interface. Furthermore, the voids generated at the ferrite–martensite interface tend to maintain their geometric shape despite the deformation process, while the voids generated at the ferrite–ferrite interface tend to elongate and close due to the ductility of this phase. Increasing the martensite volume fraction facilitates a complex deformation process in the ferrite grains. As a result, the martensite grains obstruct plastic flow, resulting in more tortuous deformation and substantial ferrite grains narrowing in the load direction (Figure 13c,f). The type of applied load also has an essential effect on the deformation

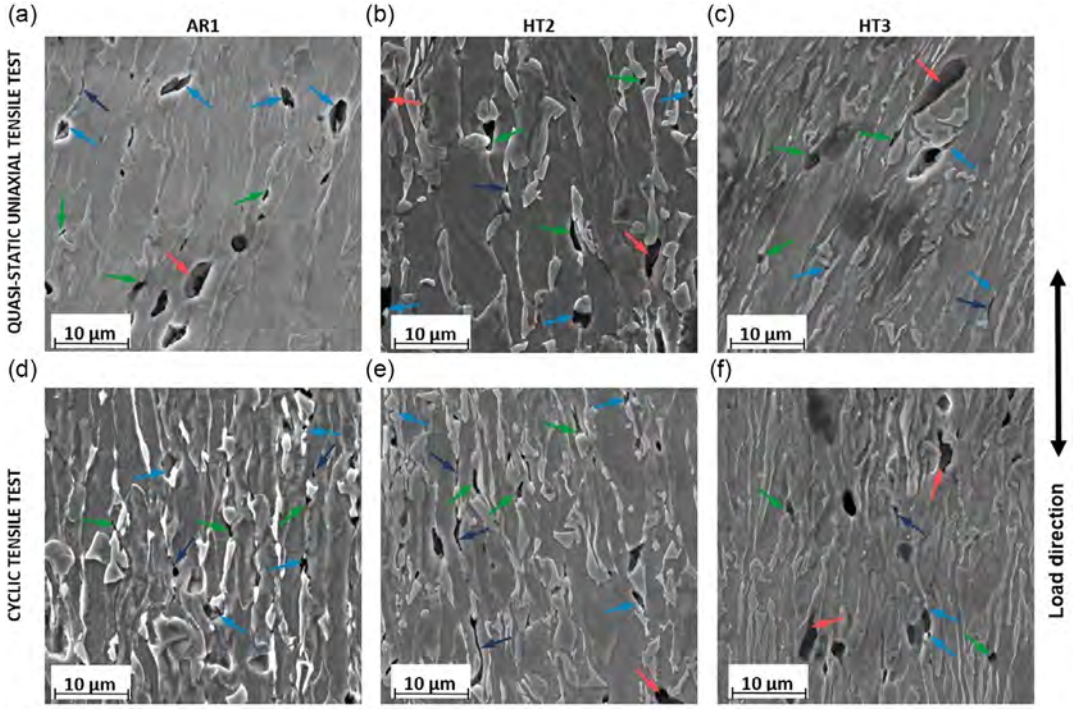

Figure 13. SEM micrographs of fracture mechanisms. The image is taken from the mid-width in the longitudinal plane of test specimens, close to the fracture zone. Arrow color convention: Red—inclusions, green—ferrite–martensite interface decohesion, dark blue—ferrite ferrite interface decohesion, and cyan—martensite fracture: a–c) quasi-static uniaxial tensile test for AR1 to HT3 steels, d–f) cyclic tensile test for AR1 to HT3 steels.

of the microstructure. The cyclic load application generated more plastic deformation and fracture in the martensite grains than the simple quasi-static uniaxial load. This effect is increased with the increase of the martensite volume fraction (Figure 13d,f).

EBSD maps allow elucidation of the microstructure evolution during the deformation process. **Figure 14**a shows the as-received microstructure by an image quality (IQ) map. In this image, the gray areas are ferrite, and the dark ones are martensite or grain boundaries. Unfortunately, in these images, it is difficult to differentiate between damage, cracks, grain boundaries, and martensite since all four factors have a low confidence index of less than 0.1, which implies that the microstructure is highly deformed in those areas, or its structure is amorphous.[75,76]

The deformation energy stored in the substrate is visualized using kernel average misorientation (KAM) maps. Because minor local strain variations are correlated to crystal orientation gradients near grain boundaries, this information allows a qualitative estimation of deformation near high-strain regions such as voids and cracks or close to severely deformed grains.[33,77] Figure 14b shows that the deformation energy is concentrated inside martensite grains or around its grain borders. This energy around martensite grains comes from the volume change in the austenite to martensite transformation during the rapid cooling process, which leads to the geometrically necessary dislocations formation at the ferrite grain boundaries. In other words, the KAM map is associated with the dislocation density and the microstructure strain energy.

Inverse pole figure (IPF) maps show the crystal orientation of each grain in the microstructure. This map allows observing the texture evolution during the deformation process (Figure 14c). By comparing the images, as shown in Figure 14, it is possible to understand why strain hardening occurs in dual-phase steels. Plastic deformation produces a reduction in grain width and an elongation in the load direction, which leads to grain boundary approximation and dislocation pile-up, which increases residual stresses that promotes grain crystallographic orientation change and therefore facilitates texture development near the fracture zone (Figure 14d). The deformed material IPF and KAM maps show multiple nonindexed zones associated with the martensite grains and the voids generated by the fracture mechanisms (Figure 14c,d). The cyclically deformed specimens were excluded from this analysis because the existing damage in the fracture zone is very high and the indexing is very low. In contrast, while KAM maps do not allow us to observe all statistically distributed dislocations,[78] they can be useful for qualitatively understanding the effect of deformation on the microstructure.

Four processes have been identified by Saeidi et al. for releasing stored strain energy throughout deformation and avoiding damage development inside the microstructure: martensite plastic deformation, substructure formation, nucleation, and development of voids, and finally, changing the overall deformation path or producing grain rotation.

Concerning martensite, as shown in Figure 13, this phase has been elongated, necked, and fractured. This process develops voids, energy dissipation, and high ductile deformation, evidenced by their low carbon content. As shown in Figure 14b, the smaller martensite grains present higher strain energy, particularly at the ferrite–martensite interface, resulting in the creation of many dislocations that create substructures inside the grains. Dislocation slip caused by the deformation process temporarily retards the damage evolution and helps release stored strain energy.[79] As the deformation process develops, the production of voids increases until coalescence and fracture surface formation occur. These voids form in places with the highest stress concentrations, including grain interfaces, martensite grains, and inclusions. Furthermore, the most visible

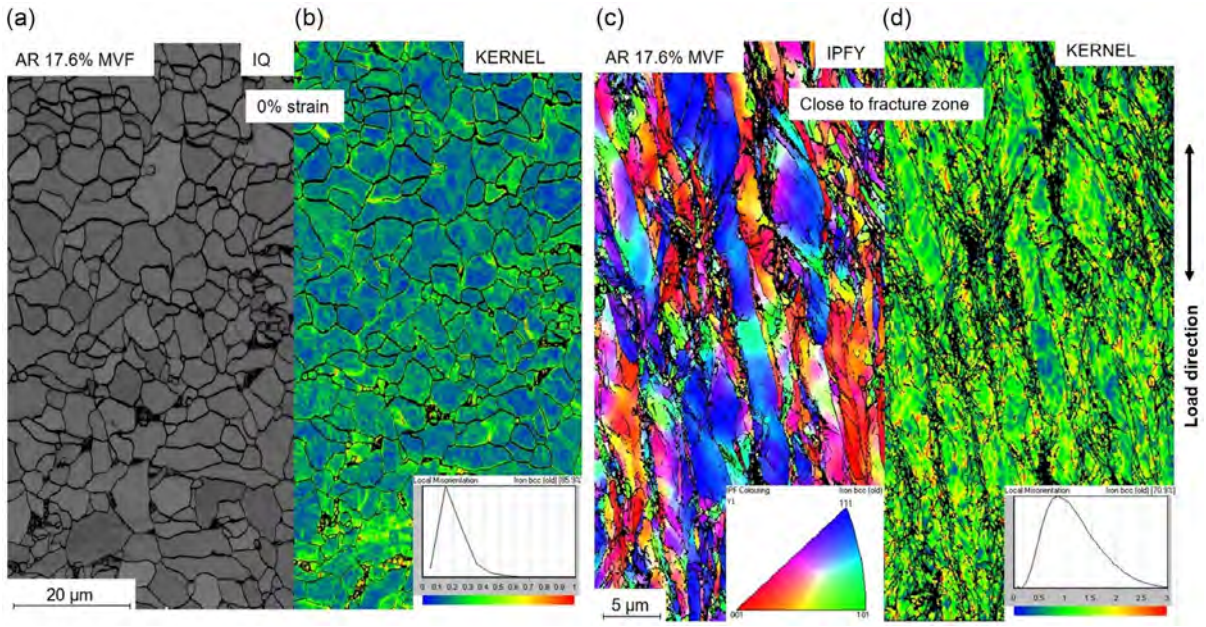

Figure 14. As-received EBSD maps of quasi-static uniaxial tensile test, the specimen is taken from the mid-width in the longitudinal plane. Undeformed specimen: a) image quality, b) Kernel average misorientation map. Deformed specimen fracture zone: c) inverse pole figure (IPFY selected as reference to load direction), d) Kernel average misorientation map.

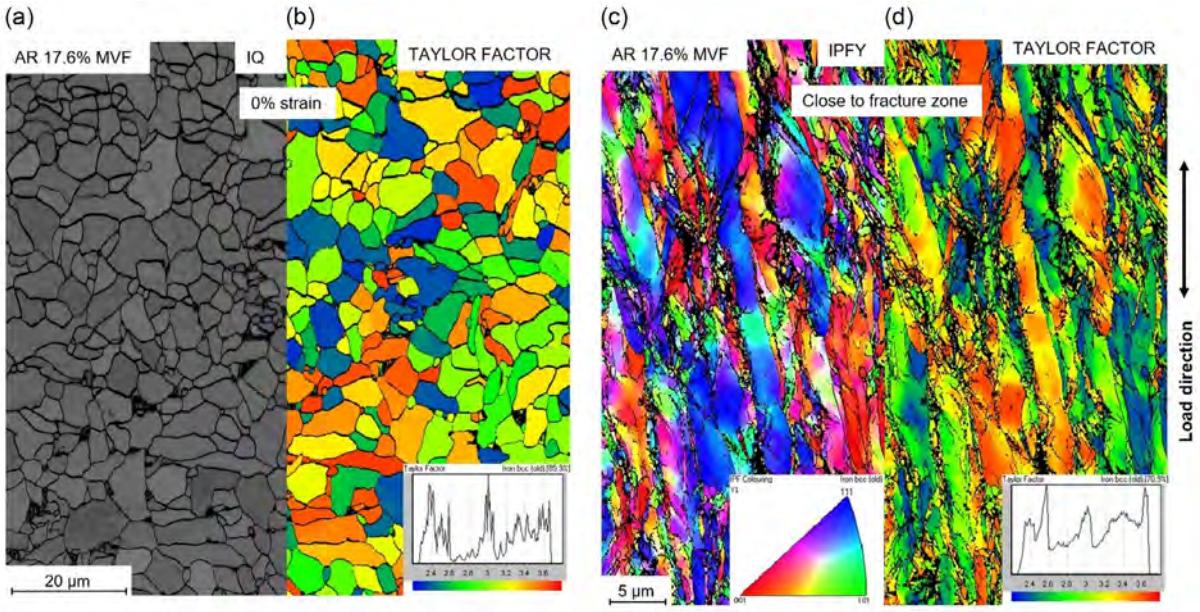

Figure 15. As-received EBSD maps of quasi-static uniaxial tensile test, the specimen is taken from the mid-width in the longitudinal plane. Undeformed specimen: a) image quality, b) Taylor factor. Deformed specimen fracture zone: c) inverse pole figure (IPFY selected as reference to load direction), d) Taylor factor.

damage generation mechanisms in the microstructure are void formation and coalescence, which are efficient methods of releasing energy during the deformation process.

Finally, the orientation stiffness is represented by the Taylor factor (TF) value.[79] A reduced value of the Taylor factor implies that the yield stress of a particular grain is low. Therefore, at lower stresses, it could be more easily deformed. A random distribution of Taylor factor values is depicted in **Figure 15**b. Furthermore, the extensively deformed region around the fracture zone, as shown in Figure 15d, should exhibit a notable trend for high Taylor factor values; instead, some soft grains have low values. The stress relaxation caused by cracks in the material could be one reason for the presence of these zones in the microstructure. Soft grains have the effect of reducing damage propagation and increasing local deformation capability. Another energy-dissipating mechanism is related to martensite and ferrite incompatibility, which results in nonuniform activation of slip systems and shear stresses, resulting in grain rotation.

The increased void amount should reduce the microstructure strength and hardness, and this should be able to be measured by the nanoindentation technique, resulting in a softening material near the fracture zone. However, nanoindentation is not an optimal technique to evaluate the microstructural damage evolution because the strain hardening near the fracture zone results in higher hardness values that are not consistent with the material softening and damage accumulation.[47,48]

4. Conclusion

This study aimed to evaluate the effect of martensite content on the mechanical response of a set of dual-phase steels with different microstructural characteristics produced by intercritical heat treatments from a hot-rolled dual-phase steel sheet. In addition, the application of quasi-static uniaxial tensile loads and cyclic deformation was evaluated on the response of the material to the damage evolution and microstructural fracture mechanisms. The findings can be summarized as follows: 1) The martensite volume fraction significantly affects the mechanical behavior of dual-phase steels with the same chemical composition. As the intercritical temperature is raised during the heat treatment, MVF increases. Moreover, with the increase of the martensite fraction, its carbon content and hardness are reduced, resulting in softer and more ductile martensite. 2) Comparing the as-received state (AR1) with the heat-treated states, the martensite mean free path decreased from 35.7 to 8.7 µm (HT2) and 2.8 µm (HT3), respectively. Simultaneously, the amount of ferrite–martensite interfaces increases with the martensite volume fraction from 17.6% (AR1) to 21.5% (HT2) and 47.5% (HT3). As a result, mobile geometrically necessary dislocations (GNDs) resulting from the stress distribution incompatibility between ferrite and martensite are produced around the grain boundaries. As observed qualitatively in the KAM maps, it can be inferred that the deformation energy is responsible for the strain hardening behavior and damage evolution on dual-phase steels. 3) Analyzing the results of the thermodynamic calculation at equilibrium conditions, austenite carbon content (and thus, martensite) between AR1 and HT3 steels decreased from 0.33 to 0.13 wt% while its nanoindentation hardness was reduced from 5.5 to 4.6 GPa. Although martensite becomes softer with increasing heat treatment temperature, dual-phase steels with higher martensite volume fraction reduce their ductility and increase their ultimate tensile strength. 4) It was found that the grain size, morphology, and distribution of martensite in the ferrite matrix all play a significant role in the strain-hardening effect of dual-phase steels. The AR1 steel presents the lowest

work-hardening rate. While the HT3 steel presents a higher initial hardening up to approximately 2% strain, from which point the HT2 material presents a more significant hardening in the quasi-static uniaxial deformation process. 5) It was possible to observe that the type of applied load (quasi-static vs. cyclic) affects the mechanical resistance of the dual-phase steel and its fracture mechanisms. Steels show lower ductility and strength under the uniaxial cyclic tensile loading condition. 6) Dual-phase steels present ductile fracture with a dimple density that is proportional to the martensite volume fraction. A higher martensite fraction is likewise related to a greater loss of stiffness and a prompt damage evolution. The three dual-phase steels show a linear relationship between damage and true strain up to 5% true strain. After 5% true strain, this linear tendency becomes stronger in AR1 steel. Furthermore, in the HT2 and HT3 treated steels, this linear trend is observed from 2% to true uniform strain. 7) It could be observed that during the plastic deformation process, the martensite grain orientation concerning the load direction has an essential effect on the ferrite plastic flow. It was seen that the higher the MVF and the number of platelet-like martensite grains obliquely oriented to the load direction, the lower the ductility of the material is. The primary void nucleation mechanisms observed are ferrite–martensite and ferrite–ferrite boundary decohesion. Other mechanisms, such as martensite fracture, can be activated due to the martensite volume fraction and distribution around ferrite grain boundaries. 8) The damage process observed in dual-phase steels can be summarized as follows: the microstructure in the as-received material presents a significant density of dislocations generated during the steel manufacturing process and due to the volume change in the austenite–martensite transformation. During the application of tensile loads, the microstructure undergoes axial deformation in the load direction. The incompatible mechanical properties of martensite and ferrite generate more dislocations, which promote strain hardening. As grains deform, they lengthen and reduce their width, increasing dislocation pile-up. Due to the increase of stored deformation energy on grain boundaries, the microstructure initiates a process of energy release through the fracture of martensite grains, the rotation of grains, the sliding of dislocations, and the formation of voids until, finally, fracture takes place.

Acknowledgements

The authors would like to thank the scientific and technical personnel of the Lehrstuhl Werkstofftechnik institute laboratories and the Ruhr-Universität Bochum for their dedicated support in implementing analytical methods and specimen preparation, especially Prof. Dr.-Ing. W. Theisen, and researchers Dr.-Ing. F. Pohl, Dr.-Ing. J. Krell, and Dr.-Ing. G. Egels. We recognize the support of the Ministerio de Ciencia Tecnología e Innovación of Colombia. We would also like to express gratitude to Mrs. I. Berns support during the project manuscripts development. Special thanks to engineers F. J. Monroy and J. J. Murillo for their insightful advice in numerically treating experimental results. Finally, to the Advanced Technical Products Supply Co., Inc., for donating ATP-641 coating.

Conflict of Interest

The authors declare no conflict of interest.

Data Availability Statement

The data that support the findings of this study are available from the corresponding author upon reasonable request.

Keywords

damage evolution, dual-phase steels, fracture mechanisms, martensite volume fraction

Received: June 2, 2022
Revised: February 15, 2023
Published online:

[1] N. Fonstein, *Advanced High Strength Sheet Steels*, Springer, East Chicago **2015**, pp. 67–181.
[2] B. Cantor, P. Grant, C. Johnston, *Automotive Engineering: Lightweight, Functional, and Novel Materials*, Taylor & Francis, New York **2008**, pp. 63–70.
[3] R. Rana, S. B. Singh, *Automotive Steels: Design, Metallurgy, Processing, and Applications*, Woodhead Publishing, Duxford **2017**, pp. 169–209.
[4] J. Zhao, Z. Jiang, *Prog. Mater. Sci.* **2018**, *94*, 174.
[5] S. Nikkhah, H. Mirzadeh, M. Zamani, *Mater. Chem. Phys.* **2019**, *230*, 1.
[6] J. Kadkhodapour, S. Schmauder, D. Raabe, S. Ziaei-Rad, U. Weber, M. Calcagnotto, *Acta Mater.* **2011**, *59*, 4387.
[7] F. Zhang, A. Ruimi, P. C. Wo, D. P. Field, *Mater. Sci. Eng., A* **2016**, *659*, 93.
[8] A. Ramazani, K. Mukherjee, U. Prahl, W. Bleck, *Metall. Mater. Trans. A* **2012**, *43*, 3850.
[9] A. Ramazani, K. Mukherjee, A. Schwedt, P. Goravanchi, U. Prahl, W. Bleck, *Int. J. Plast.* **2013**, *43*, 128.
[10] Y. Mazaheri, A. H. Jahanara, M. Sheikhi, A. G. Kalashami, *Mater. Sci. Eng., A* **2019**, *761*, 138021.
[11] T. Nanda, V. Singh, V. Singh, A. Chakraborty, S. Sharma, *Proc. Inst. Mech. Eng., Part L: J. Mater.: Des. Appl.* **2019**, *233*, 209.
[12] M. Y. Demeri, *Advanced High-Strength Steels: Science, Technology, and Applications*, ASM International, Ohio **2013**, pp. 95–106.
[13] J. B. Seol, J. E. Jung, Y. W. Jang, C. G. Park, *Acta Mater.* **2013**, *61*, 558.
[14] M. Calcagnotto, D. Ponge, D. Raabe, *Metall. Mater. Trans. A* **2012**, *43*, 37.
[15] L. Y. Zhou, D. Zhang, Y. Z. Liu, *Int. J. Miner. Metall. Mater.* **2014**, *21*, 755.
[16] J. Drumond, O. Girina, J. F. da Silva Filho, N. Fonstein, C. A. de Oliveira, *Metall. Microstruct. Anal.* **2012**, *1*, 217.
[17] J. F. D. S. Filho, C. A. S. D. Oliveira, N. Fonstein, O. Girina, F. J. F. Miranda, J. Drumond, E. A. Serafim, C. R. M. Afonso, *Mater. Res.* **2016**, *19*, 258.
[18] M. Calcagnotto, D. Ponge, D. Raabe, *Mater. Sci. Eng., A* **2010**, *527*, 7832.
[19] C. Nikhare, P. Hodgson, M. Weiss, *Mater. Sci. Eng., A* **2011**, *528*, 3010.
[20] G. Avramovic-Cingara, C. Saleh, M. Jain, D. Wilkinson, *Metall. Mater. Trans. A* **2009**, *40*, 3117.
[21] M. Calcagnotto, D. Ponge, D. Raabe, *ISIJ Int.* **2012**, *52*, 874.
[22] J. Zhang, H. Di, Y. Deng, R. Misra, *Mater. Sci. Eng., A* **2015**, *627*, 230.
[23] H. R. Pakzaman, S. S. Banadkouki, *Metall. Microstruct. Anal.* **2021**, *10*, 610.
[24] D. Avendaño-Rodríguez, J. D. Granados, E. Espejo-Mora, L. Mujica-Roncery, R. Rodríguez-Baracaldo, *J. Eng. Sci. Technol. Rev.* **2018**, *11*, 174.

[25] C. P. Velasquez, D. A. Rodriguez, C. N. Tovar, L. M. Roncery, R. R. Baracaldo, *Int. J. Automot. Mech. Eng.* **2020**, *17*, 8086.
[26] H. Farivar, S. Richter, M. Hans, A. Schwedt, U. Prahl, W. Bleck, *Mater. Sci. Eng., A* **2018**, *718*, 250.
[27] J. Samei, L. Zhou, J. Kang, D. S. Wilkinson, *Int. J. Plast.* **2019**, *117*, 58.
[28] K. Ismail, A. Perlade, P. J. Jacques, T. Pardoen, *Acta Mater.* **2021**, *207*, 116700.
[29] K. Ismail, A. Perlade, P. J. Jacques, T. Pardoen, L. Brassart, *Int. J. Plast.* **2019**, *118*, 130.
[30] C.-H. Hsueh, S. Schmauder, C.-S. Chen, K. K. Chawla, N. Chawla, W. Chen, Y. Kagawa, *Handbook of Mechanics of Materials*, Vol. *2*, Springer Nature, Singapore **2019**, pp. 1127–1156.
[31] G. Avramovic-Cingara, Y. Ososkov, M. K. Jain, D. S. Wilkinson, *Mater. Sci. Eng., A* **2009**, *516*, 7.
[32] N. Saeidi, F. Ashrafizadeh, B. Niroumand, F. Barlat, *Steel Res. Int.* **2014**, *85*, 1386.
[33] H. Ashrafi, M. Shamanian, R. Emadi, E. Ghassemali, *Acta Metall. Sin.* **2020**, *33*, 299.
[34] M. Jafari, S. Ziaei-Rad, N. Saeidi, M. Jamshidian, *Mater. Sci. Eng., A* **2016**, *670*, 57.
[35] E. E. Asik, E. S. Perdahcıoğlu, A. H. van den Boogaard, *Mater. Sci. Eng., A* **2019**, *739*, 348.
[36] C. Du, J. P. Hoefnagels, R. Vaes, M. G. Geers, *Scr. Mater.* **2016**, *120*, 37.
[37] M. Mazinani, W. Poole, *Metall. Mater. Trans. A* **2007**, *38*, 328.
[38] J. Kadkhodapour, A. Butz, S. Z. Rad, *Acta Mater.* **2011**, *59*, 2575.
[39] C. F. Kusche, A. Dunlap, F. Pütz, C. Tian, C. Kirchlechner, A. Aretz, A. Schwedt, T. Al-Samman, S. Münstermann, S. Korte-Kerzel, *Prod. Eng.* **2020**, *14*, 95.
[40] K. Isik, G. Gerstein, T. Clausmeyer, F. Nürnberger, A. E. Tekkaya, H. J. Maier, *Steel Res. Int.* **2016**, *87*, 1583.
[41] H. Toda, A. Takijiri, M. Azuma, S. Yabu, K. Hayashi, D. Seo, M. Kobayashi, K. Hiray, a, ma, A. Takeuchi, K. Uesugi, *Acta Mater.* **2017**, *126*, 401.
[42] P. Zhao, Y. Sun, J. Jiao, G. Fang, *Eng. Fract. Mech.* **2020**, *230*, 106967.
[43] N. Bonora, A. Ruggiero, D. Gentile, S. D. Meo, *Strain* **2011**, *47*, 241.
[44] C. Landron, O. Bouaziz, E. Maire, J. Adrien, *Scr. Mater.* **2010**, *63*, 973.
[45] C. Landron, O. Bouaziz, E. Maire, J. Adrien, *Acta Mater.* **2013**, *61*, 6821.
[46] H. Azizi, J. Samei, H. S. Zurob, D. S. Wilkinson, D. Embury, *Mater. Sci. Eng., A* **2022**, *833*, 142582.
[47] C. C. Tasan, J. P. M. Hoefnagels, M. G. D. Geers, *Acta Mater.* **2009**, *57*, 4957.
[48] C. C. Tasan, J. P. Hoefnagels, M. G. Geers, *Scr. Mater.* **2010**, *63*, 316.
[49] C. C. Tasan, J. P. M. Hoefnagels, M. G. D. Geers, *Acta Mater.* **2012**, *60*, 3581.
[50] M. Alves, J. Yu, N. Jones, *Comput. Struct.* **2000**, *76*, 703.
[51] K. Ichinose, K. Fukuda, K. Gomi, K. Taniuchi, M. Sano, *J. Test. Eval.* **2001**, *29*, 529.
[52] S. P. Tsiloufas, R. L. Plaut, *Mater. Sci. Appl.* **2012**, *03*, 745.
[53] J. Lemaitre, *J. Eng. Mater. Technol.* **1985**, *107*, 83.
[54] L. Sun, R. H. Wagoner, *Int. J. Plast.* **2011**, *27*, 1126.
[55] A. Govik, R. Rentmeester, L. Nilsson, *Mater. Sci. Eng., A* **2014**, *602*, 119.
[56] Y. X. Zhu, Y. L. Liu, H. Yang, H. P. Li, *Mater. Des.* **2012**, *42*, 245.
[57] H. Kim, C. Kim, F. Barlat, E. Pavlina, M. G. Lee, *Mater. Sci. Eng., A* **2013**, *562*, 161.
[58] ASTM-E8, *Standard Test Methods for Tension Testing of Metallic Materials*, ASTM International, West Conshohocken, Pensilvania **2016**.
[59] ASTM-E466, *Standard Practice for Conducting Force Controlled Constant Amplitude Axial Fatigue Tests of Metallic Materials*, ASTM International, West Conshohocken, Pensilvania **2015**
[60] Y. Lu, H. Yu, X. Cai, Y. Rong, R. Sisson, in *23rd Int. Federation of Heat Treatment and Surface Engineering Congress 2016, IFHTSE 2016*, Savannah, GA, USA **2016**, pp. 18–21.
[61] J. J. Murillo-Barraza, D. F. Avendaño-Rodríguez, W. A. Suárez-Ortiz, *Identificación automática de fases de la microestructura de aceros de fase dual a partir del procesamiento digital de imágenes*, Fundación Universidad de América, Bogotá **2020**, https://hdl.handle.net/20.500.11839/8217 (accessed: May 2022).
[62] ASTM-E112, *Standard Test Methods for Determining Average Grain Size*, ASTM International, West Conshohocken, Pensilvania **2013**, https://doi.org/10.1520/E0112-13.
[63] ASTM-E1245, *Standard Practice for Determining the Inclusion or Second-Phase Constituent Content of Metals by Automatic Image Analysis*, ASTM International, West Conshohocken, Pensilvania **2003**.
[64] ASTM-E1382, *Standard Test Methods for Determining Average Grain Size Using Semiautomatic and Automatic Image Analysis*, ASTM International, West Conshohocken, Pensilvania **2015**.
[65] ASTM-E646, *Standard Test Method for Tensile Strain-Hardening Exponents (n-Values) of Metallic Sheet Materials*, ASTM International, West Conshohocken, Pensilvania **2016**.
[66] Y. Mazaheri, A. Kermanpur, A. Najafizadeh, *Mater. Sci. Eng., A* **2015**, *639*, 8.
[67] N. Gorain, M. G. Walunj, M. K. Soni, B. R. Kumar, *Arch. Civ. Mech. Eng.* **2020**, *20*, 1.
[68] L. Y. Wang, Y. X. Wu, W. W. Sun, Y. Bréchet, L. Brassart, A. Arlazarov, C. R. Hutchinson, *Acta Mater.* **2020**, *199*, 613.
[69] X. Zhang, H. Wang, T. Hickel, J. Rogal, Y. Li, J. Neugebauer, *Nat. Mater.* **2020**, *19*, 849.
[70] H. Ashrafi, M. Shamanian, R. Emadi, N. Saeidi, *Trans. Indian Inst. Met.* **2017**, *70*, 1575.
[71] D. Das, P. P. Chattopadhyay, *J. Mater. Sci.* **2009**, *44*, 2957.
[72] H. Seyedrezai, A. K. Pilkey, J. D. Boyd, *Mater. Sci. Eng., A* **2014**, *594*, 178.
[73] X. Xue, J. Liao, G. Vincze, A. B. Pereira, F. Barlat, *Int. J. Mech. Sci.* **2016**, *117*, 1.
[74] S. F. Lajarin, C. P. Nikhare, P. V. P. Marcondes, *J. Braz. Soc. Mech. Sci. Eng.* **2018**, *40*, 1.
[75] A. Laureys, T. Depover, R. Petrov, K. Verbeken, *Mater. Charact.* **2016**, *112*, 169.
[76] K. Radwański, *Steel Res. Int.* **2015**, *86*, 1379.
[77] N. Saeidi, F. Ashrafizadeh, B. Niroumand, F. Barlat, *J. Mater. Eng. Perform.* **2014**, *24*, 53.
[78] N. Wang, Y. Chen, G. Wu, Q. Zhao, Z. Zhang, L. Zhu, J. Luo, *Mater. Sci. Eng., A* **2022**, *836*, 142728.
[79] N. Saeidi, F. Ashrafizadeh, B. Niroumand, F. Barlat, *Mater. Des.* **2015**, *87*, 130.